Supporting Information for

Polymerization-Like Kinetics on Self-Assembly of Colloidal Nanoparticles into Supracolloidal Polymers

Xiaodong Ma, Yaru Zhou, Liangshun Zhang, Jiaping Lin* and Xiaohui Tian*

Shanghai Key Laboratory of Advanced Polymeric Materials, State Key Laboratory of Bioreactor Engineering, Key Laboratory for Ultrafine Materials of Ministry of Education, School of Materials Science and Engineering, East China University of Science and Technology, Shanghai 200237, China

*E-mail: zhangls@ecust.edu.cn (Zhang L.); jlin@ecust.edu.cn (Lin J.)

Contents

Part A: Computational model and coarse-grained mapping

Dissipative Particle Dynamics In the model, DPD beads represent a group of atoms or a volume of fluids and interact through short-ranged potentials.[S1] The beads labeled by index i=1, 2,···, N occupy continuous positions $\mathbf{r}_i$ and velocities $\mathbf{v}_i$. The temporal evolution of i-th bead is described by the Newton's motion equations $\mathrm{d}r_i/\mathrm{d}t = v_i$ and $m_i \mathrm{d}v_i/\mathrm{d}t = f_i$, where m_i is bead mass. The total force $\mathbf{f}_i$ on the i-th bead is sum of conservative force F_{ij}^{C}, dissipative force F_{ij}^{D} and random force F_{ij}^{R}, *i.e.*, $$f_i = \sum_{j \neq i} \left(F_{ij}^{\mathrm{C}} + F_{ij}^{\mathrm{D}} + F_{ij}^{\mathrm{R}} \right)$$. The conservative force for non-bonded beads is expressed as

$$F_{ij}^{\mathrm{C}} = \begin{cases} a_{ij} \left(1 - r_{ij}/r_{\mathrm{c}} \right) \hat{r}_{ij} & (r_{ij} < r_{\mathrm{c}}) \\ 0 & (r_{ij} \geq r_{\mathrm{c}}) \end{cases}$$

(S1)

where the interaction parameter a_{ij} determines maximum repulsion and r_{c} represents cutoff radius of interaction. The dissipative and random forces are respectively given by $F_{ij}^{\mathrm{D}} = -\gamma \omega^{\mathrm{D}}(r_{ij}) \left(\hat{r}_{ij} \cdot v_{ij} \right) \hat{r}_{ij}$ and $F_{ij}^{\mathrm{R}} = \sigma \omega^{\mathrm{R}}(r_{ij}) \xi_{ij} \hat{r}_{ij} / \sqrt{\delta t}$, where $\mathbf{r}_{ij} \equiv \mathbf{r}_i - \mathbf{r}_j$ and $\mathbf{v}_{ij} \equiv \mathbf{v}_i - \mathbf{v}_j$. r_{ij} is relative displacement between the i-th and j-th beads and $\hat{r}_{ij} = r_{ij}/r_{ij}$ is the corresponding unit vector. The friction coefficient γ and the noise amplitude σ govern magnitude of dissipative forces and intensity of random forces, respectively. The weight functions $\omega^{\mathrm{D}}(r_{ij})$ and $\omega^{\mathrm{R}}(r_{ij})$ respectively determine range of dissipative and random forces and vanish for $r_{ij} \geq r_{\mathrm{c}}$. The term ξ_{ij} is a random variable with zero mean and unit variance. δt is time step of simulations. In addition, constraints between the connected beads within polymer chains are described by simple harmonic force $F_{ij}^{\mathrm{S}} = -C^{\mathrm{S}} \left(r_{ij} - r_{\mathrm{eq}} \right) \hat{r}_{ij}$, where C^{S} and r_{eq} respectively denote spring constant and equilibrium bond length.

The interaction parameter a_{ij} in Eq. (S1) depends on the underlying atomistic interactions according to linear relationship with the Flory-Huggins parameter χ_{ij}[S1]

$$a_{ij} = a_{ii} + 3.50\chi_{ij} \quad (\rho = 3) \tag{S2}$$

Here, a_{ii}=25 denotes the interaction parameter between the like beads and ρ=3 is number density of system. The Flory-Huggins parameters between distinct polymer beads are estimated from the Hildebrand solubility parameters δ through following formula $\chi_{ij} = \dfrac{V_{\text{bead}}}{k_B T}(\delta_i - \delta_j)^2$,[S2] where $k_B T$ is the thermal energy and V_{bead} is volume of coarse-grained beads. The material-specific solubility parameters are deduced from the atomistic molecular dynamics simulations through expression $\delta = \sqrt{E_{\text{coh}}/V}$, where E_{coh} and V respectively represent cohesive energy and volume of simulation box at equilibrium. It should be pointed out that volume fractions of polymers in dilute solution are extremely smaller than those of solvent molecules. Under this condition, the Flory-Huggins parameters between solvent and polymer beads are estimated by the modified equation of binary mixture $\chi_{ij} = \dfrac{V_{\text{bead}}}{k_B T}\Delta E_{\text{mix}}$.[S3]

Here, ΔE_{mix} is the mixing energy of binary mixture calculated from expression $\Delta E_{\text{mix}} = \varphi_S (E_{\text{coh}}/V)_S + \varphi_P (E_{\text{coh}}/V)_P - (E_{\text{coh}}/V)_{S-P}$, where $(E_{\text{coh}}/V)_{S\text{-}P}$ and $(E_{\text{coh}}/V)_{S(P)}$ respectively are cohesive energy density of polymer solution and pure solvents (polymers). φ_S and φ_P are volume fractions of solvents and polymers, respectively. In the case of dilute solution, $\varphi_S \approx 1$ and $\varphi_P \approx 0$ are used.

Coarse-Grained Mapping In the mesoscopic model, realistic polymeric molecules are generally represented by the coarse-grained chains. In this work, polystyrene-*block*-polybutadiene-*block*-poly(methylmethacrylate)(PS-*b*-PB-*b*-PMMA) used in the Müller's group serves as a reference for our model polymers.[S4] Two types of selective solvents (*i.e.*, N,N-dimethylacetamide (DMAc) and mixed acetone/isopropanol solvents) are utilized to

prepare hierarchically self-assembled superstructures of triblock terpolymers. As a consequence, our model systems include five different species of coarse-grained beads. Basic assumption for the coarse-grained mapping is that all beads in the mesoscopic model are of the same or similar volume (*i.e.*, V_{bead}=5200.0 Å^3 in this work). Figure 1a of main text schematically illustrates the mapping scheme for experimental system, and Table S1 lists molecular parameters of triblock terpolymers and selective solvents. 34 DMAc molecules are taken together and grouped into one coarse-grained bead coded by S' bead. The mixed solvents encompassing 25 acetone and 17 isopropanol molecules are coarse-grained into one S bead. One bead in the triblock terpolymers roughly contains 32 styrene monomers (A bead), 54 butadiene monomers (B bead) or 37 methylmethacrylate monomers (C bead).

Computational parameters Based on the coarse-grained mapping of triblock terpolymers and solvent molecules, we perform the atomistic molecular dynamics simulations of pure and binary systems to deduce the Flory-Huggins parameters χ_{ij} between distinct coarse-grained beads. Either pure component or dilute solution is constructed in simulation box with periodic boundary conditions. The high-quality COMPASS force field is chosen (Forcite module, Materials Studio V5.5, Accelrys Ltd.). At the beginning stage of simulation, energy minimization for initial configuration is performed to eliminate unfavorable contacts and relax unfavorable structures of polymer chains. Subsequently, the atomistic molecular dynamics simulation is carried out under the isothermal-isobaric ensemble for 1 ns with integration time step 1 fs. Constant temperature T=298 K and pressure P=1.0 bar are controlled through the Berendsen thermostat and barostat. Next, the solubility parameters δ or the mixing energies ΔE_{mix} are calculated *via* cohesive energy E_{coh} and box volume V at

equilibrium (Table S1 and S2), which are determined by sampling the system and collecting the data every 500 ps. Then, the Flory-Huggins parameters χ_{ij} for the coarse-grained beads are gained. Finally, Eq. (S2) is utilized to estimate the interaction parameter a_{ij} of conservative force, which is listed in Table S3. In particular, the S' beads are a good solvent for the A and C blocks, whereas a poor solvent for the B blocks. As the S' beads are replaced by the S beads, the solvent quality is altered and the A blocks become solvophobic.

According to the coarse-grained model and the interaction parameters, the DPD simulations are performed in cubic boxes with edge size $L=60.0r_c$ under the periodic boundary conditions at constant number density $\rho=3$. The noise amplitude σ is set as 3.0. The spring constant C^S is fixed at 4.0. Note that all the units in DPD simulations are scaled by bead mass m, cutoff radius r_c and thermal energy k_BT. Since the volume V_{bead} of coarse-grained beads is chosen as 5200.0 Å^3 in this work, the cutoff radius r_c has a value of $r_c \equiv (\rho V_{bead})^{1/3} = 25.0$ Å. According to Groot's idea, [S5] the simulation time (in units of time unit τ) matches the real time *via* diffusion coefficient of water. The diffusion coefficient of water beads in the simulations is $D_{sim} = 0.1707 r_c^2/\tau$, and its relation with the diffusion coefficients D_{exp} in experiments is expressed as $D_{sim}=D_{exp}/N_w$. Herein, N_w is the number of water molecules in a coarse-grained bead and the cutoff radius r_c has a value of $r_c=(\rho V_w N_w)^{1/3}$, where $V_w=30.0$ Å^3 represents the volume of water beads. Consequently, the time unit is given by $\tau = 0.1707 r_c^2 N_w/D_{exp} = 14.1 N_w^{5/3} \, ps$, where D_{exp} has a value of 2.43×10^{-9} m^2/s. In our simulations, the value of N_w is obtained by N_w=5200Å^3/30Å$^3 \approx$173, leading to the time unit $\tau \approx 75.0$ ns. The motion equations are integrated by the modified Velocity-Verlet algorithm,

where the time step is set as δt=0.02τ=1.5 ns. The total simulation time of 2×10^6 steps has a value of t=2×10^6×1.5 ns=3000.0 μs.

To ensure that the observed structures are not accidental, the DPD simulations for given parameter settings are repeated 10 times using different initial configurations and random numbers. Furthermore, we also carry out the simulations with various box sizes to check effect of finite size. From Figure S1, it is demonstrated that the self-assembly kinetics of nanostructures is weakly influenced by the size of simulation boxes under the condition of L>45.0r_c.

Table S1. Molecular parameters of polymers and solvent molecules in the self-assembly system

	Molecular Weight M (g/mol)	Density ρ (g/cm³)	Monomer Volume[a] V_M (Å³)	Monomer Number per DPD Bead[b]	Solubility Parameter[c] δ ((J/cm³)^{1/2})	Solubility Parameter[d] δ ((J/cm³)^{1/2})
PS	104	1.05	164	32	19.87	15.6~21.1
PB	54	0.93	96	54	16.61	16.5~17.6
PMMA	100	1.18	140	37	18.52	18.4~19.7
DMAc	87	0.94	153	34	–	–
Mix[e]	59	0.79	124	42	–	–

a. Monomer volume is calculated by using molecular weight and density at the ambient temperature.

b. Monomer number per DPD bead is obtained from the expression $N_{monomer}=V_{bead}/V_M$, where V_{bead} is set as 5200.0 Å³ in our coarse-grained mapping.

c. Solubility parameter is derived from the atomistic molecular dynamics simulations.

d. Reference value of solubility parameter is collected from Ref. S6.

e. Mix represents the mixed acetone/isopropanol (volume fraction 60%/40%) solvent.

Table S2. Cohesive energy density E_{coh}/V of dilute polymer solution

E_{coh}/V (J/cm³)	DMAc[a]	Mix[b]
PS	516.51	424.22
PB	504.19	415.19
PMMA	516.61	427.58

a. Cohesive energy density for pure DMAc is $(E_{coh}/V)_{DMAc}$=517.17 J/cm³.

b. Mix represents the mixed acetone/isopropanol (volume fraction 60%/40%) solvent. In our simulations, mixture of solvent molecules is simplified as one type of bead due to similarity of their physicochemical properties for triblock terpolymers. Cohesive energy density for the mixed solvent is $(E_{coh}/V)_{Mix}$=427.59 J/cm³.

Table S3. Interaction parameters a_{IJ} between I- and J-type beads for triblock terpolymers in dilute solution. The Flory-Huggins parameters χ_{IJ} calculated from the atomistic molecular dynamics are also shown in parentheses.

$a_{IJ}(\chi_{IJ})$	S' (DMAc)	S (Mix)[a]	A (PS)	B (PB)	C (PMMA)
S' (DMAc)	25.0 (0.0)	–	27.9 (0.83)	82.4 (16.41)	27.5 (0.71)
S (Mix)[a]		25.0 (0.0)	40.0 (4.26)	79.8 (15.67)	25.0 (0.01)
A (PS)			25.0 (0.0)	71.9 (13.43)	33.1 (2.30)
B (PB)				25.0 (0.0)	41.1 (4.61)
C (PMMA)					25.0 (0.0)

a. Mix represents the mixed acetone/isopropanol (volume fraction 60%/40%) solvent.
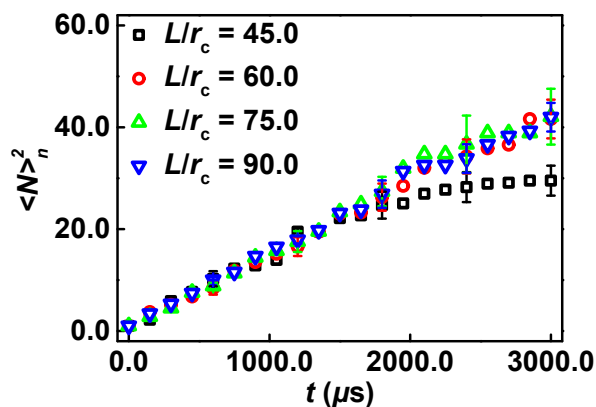

Figure S1. Temporal evolution of square $\langle N \rangle_n^2$ of average number of colloidal monomers in the supracolloidal polymers for various edge sizes L of simulation boxes. The error bars stand for the standard deviations.

Part B. First-step assembly of triblock terpolymers

In the first-step assembly, the DPD simulations start from configuration of polymer chains randomly dispersed in the S' solvents. The volume fraction of triblock terpolymers is set as 0.1 and the values of interaction parameters a_{IJ} between the I- and J-type beads are listed in Table S3. Because the S' beads are selective to the A and C blocks, the triblock terpolymers spontaneously associate into spherical micelles with B cores and mixed A/C coronas, which are illustrated in upper panels of Figure S2. The bottom panels of Figure S2 show the probability distributions $P(n_{chain})$ of chain number n_{chain} in each micelle. The histograms of chain number exhibit a broad distribution with a single peak, corresponding to the thermodynamically preferable chain number in the micelles under specific conditions. For the micellar structures of $A_xB_yC_z$ triblock terpolymers with block length ratio $x/y>1.0$, the peak positions of distributions can be tuned by the block length ratio. For the case of $A_xB_yC_z$ triblock terpolymers with $x/y<1.0$, the peak locations of distributions are nearly the same, implying that the triblock terpolymers with long solvophobic blocks self-assemble into the micelles with similar shape and size (*i.e.*, $n_{chain}\approx60$ at the near-equilibrium configuration of micelles).[S7]
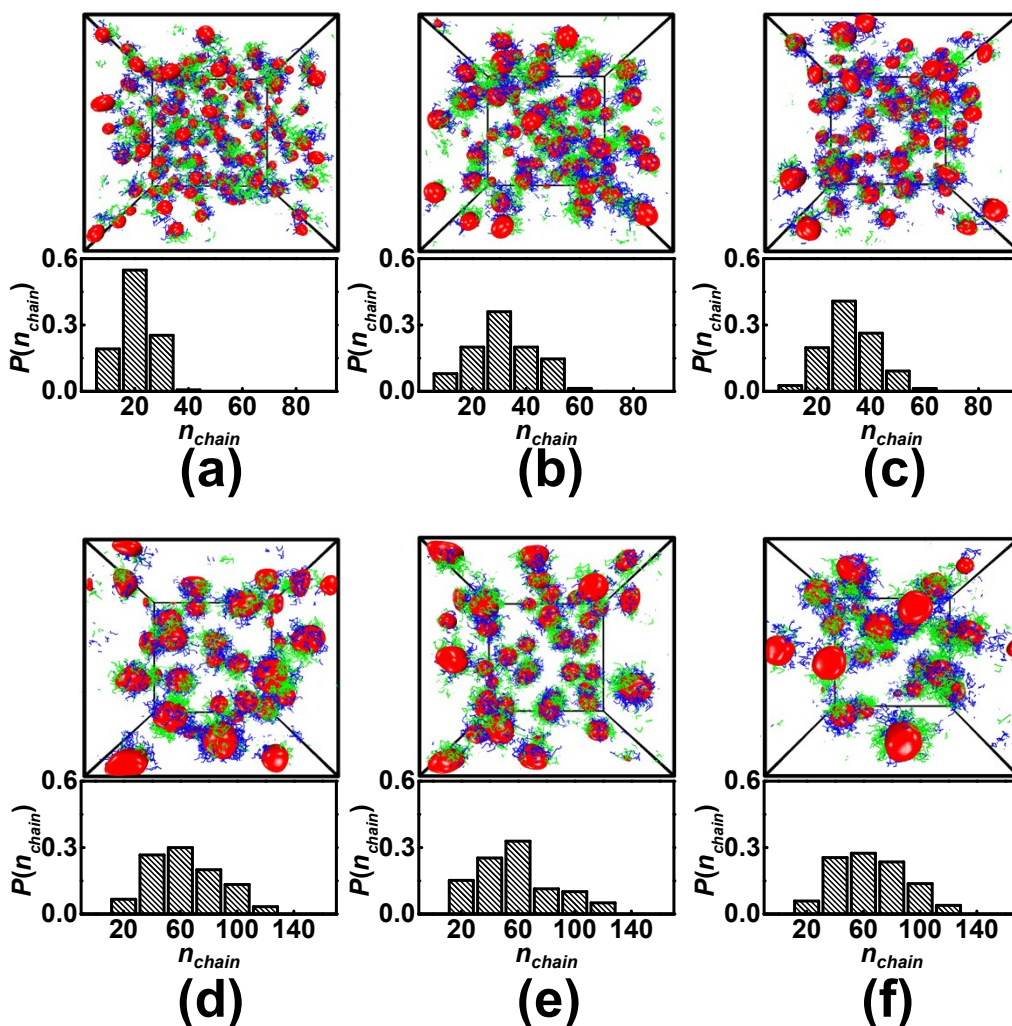
Figure S2. Self-assembly behavior of $A_xB_yC_z$ triblock terpolymer/S' solvent system in the first-step assembly. (Upper panels) Aggregate morphologies of $A_xB_yC_z$ triblock terpolymers in the selective S' solution. (Lower panels) Probability distributions $P(n_{chain})$ of chain number n_{chain} in each micelle. (a) $A_{10}B_3C_9$ (corresponds to $PS_{306}PB_{151}PMMA_{340}$ in experiments), (b) $A_{11}B_6C_{10}$ ($PS_{337}PB_{333}PMMA_{369}$), (c) $A_9B_6C_{12}$ ($PS_{277}PB_{333}PMMA_{430}$), (d) $A_{11}B_{14}C_{11}$ ($PS_{363}PB_{765}PMMA_{389}$), (e) $A_9B_{11}C_8$ ($PS_{283}PB_{596}PMMA_{304}$) and (f) $A_{12}B_{15}C_{14}$ ($PS_{374}PB_{819}PMMA_{509}$). The volume fraction of polymer chains is set as 0.1 and the values of interaction parameters are presented in Table S3. The green, red and blue colors represent the solvophilic A blocks, solvophobic B domains and solvophilic C blocks, respectively.

Part C: Second-step assembly of triblock terpolymers

In the second-step assembly, the initial configurations of $A_xB_yC_z$ triblock terpolymers are the final states of spherical micelles obtained from the simulations of first-step assembly, which is depicted in Figure 1b of main text. However, the S' solvent beads are replaced by the S beads. The environmental change of spherical micelles in the DPD simulations is mainly manifested through the parameter setting of interaction parameter a_{AS}=40.0, indicating that the solvent-sensitive A blocks become solvophobic. As shown in Table S3, the slight variations of interaction parameters between the B or C blocks and solvent beads suggest the maintenance of solvent quality for the B and C blocks.

Figure S3 illustrates the morphological evolution of spherical micelles dispersed in the S solvents at the early stage of second-step assembly. The initial states of spherical micelles are composed of the B-rich solvophobic cores as well as the mixed A and C solvophilic coronas. The change of solvent quality for the solvent-sensitive A blocks induces the collapse of A blocks to form patch-like structures on the outer surfaces of B core, while the solvophilic C blocks remain swollen by the S solvent. To reduce the surface of solvophobic A domains, the smaller A patches gradually fuse into the larger patches decorating on the B cores due to the soft and dynamic characteristics of molecular self-assembled nanostructures (Figure S3). It should be pointed out that the valence of nanostructures (*i.e.*, number of patches) is definitely determined by the length ratio *x/y* of solvophobic blocks. As the solvophobic B blocks are not dominant, the spherical micelles with mixed A/C corona evolve into the monovalent Janus-type nanostructures with one attractive A patch and one repulsive C corona on opposing sides of the B core (Figure S3a). Increasing the length of B blocks leads to formation of divalent

nanostructures with two attractive A patches on opposing sides of B cores and the repulsive C blocks emanating radially from the B core (Figure S3b). It should be mentioned that the valence of nanoparticles shows slight polydispersity depending upon their size (inset of bottom panels in Figure S4). For the triblock terpolymers with length ratio x/y>1, the spherical micelles evolve into the monovalent colloidal nanoparticles, which are independent on the size of micelles. However, for the triblock terpolymers with length ratio x/y<1, the spherical micelles predominantly form the divalent colloidal nanoparticles, while the small micelles with chain number n_{chain}<30 form the monovalent colloidal nanoparticles.

To further minimize the energy contribution from unfavorable A patch/solvent interfaces, the colloidal nanoparticles undergo next-level assembly to yield complicated superstructures with controllable morphologies and predictable internal components. Figure S4 displays the self-assembled superstructures of colloidal nanoparticles prepared by the $A_xB_yC_z$ triblock terpolymers with various length ratios x/y of A to B blocks. Insets show the typical configurations of triblock terpolymers in the superstructures. As the value of x/y is larger than 1.0, the monovalent Janus-type nanoparticles serve as building units to further self-assemble into the spherical multicompartment superstructures (Figure S4a-S4c). Therein, the B compartments stabilized by the C chains reside on the solvophobic A domain. However, the $A_xB_yC_z$ triblock terpolymers with length ratio x/y<1.0 finally form the linear multicompartment superstructures *via* intermediate state of divalent colloidal nanoparticles (Figure S4d-S4f). They usually possess the terminal A compartments and the laterally stabilizing C chains, which only emanate from the non-terminal B compartments (insets of Figure S4d-S4f).

A simple clustering algorithm is applied to ascertain number n_B of B compartments in each superstructure. The bottom panels of Figure S4 display the probability distributions $P(n_B)$ of B compartment number in each superstructure. In the case of $A_xB_yC_z$ triblock terpolymers with length ratio $x/y>1.0$, the probability distributions of B compartment number exhibit a single peak. For instance, the $A_{10}B_3C_9$ triblock terpolymers form more than 40% Maltese cross superstructures with four B compartments (Figure S4a), whereas the $A_9B_6C_{12}$ molecules yield ~80% hamburger superstructures with BAB sequence of solvophobic compartments (Figure S4c). In the case of $A_xB_yC_z$ triblock terpolymers with length ratio $x/y<1.0$, the dominant populations are the inverse hamburger micelles with ABA sequence of solvophobic compartments (Figure S4d-S4f). Such micelles have the capability to further self-assemble into the linear multicompartment superstructures with repeating unit of ABA sequence. The linear superstructures are referred to as supracolloidal polymers.

We also perform a series of DPD simulations for the case of $A_9B_yC_8$ triblock terpolymers with various lengths of B blocks. As shown in Figure S5, the polymer molecules with longer B blocks hierarchically self-assemble into the linear superstructures. As the lengths of A and B blocks are comparable, mixture of linear and spherical superstructures is identified. The triblock terpolymers with shorter B blocks hierarchically self-assemble into the spherical superstructures with controllable numbers of B compartments, which are tuned by the molecular parameters of polymers.
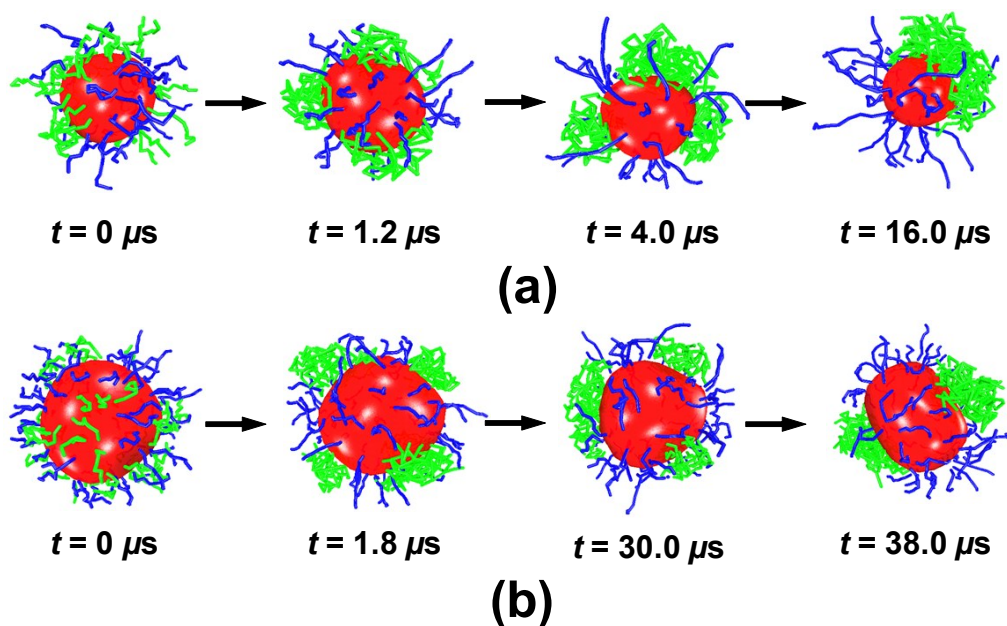
$t = 0$ μs $t = 1.2$ μs $t = 4.0$ μs $t = 16.0$ μs

(a)

$t = 0$ μs $t = 1.8$ μs $t = 30.0$ μs $t = 38.0$ μs

(b)

Figure S3. Representative snapshots of morphological evolution at the early stage of second-step assembly for various $A_xB_yC_z$ triblock terpolymers in selective S solution. (a) $A_{11}B_6C_{10}$ triblock terpolymers with block length ratio $x/y \approx 1.8$, and (b) $A_9B_{14}C_8$ triblock terpolymers with block length ratio $x/y \approx 0.6$. The initial configurations at $t=0$ μs are the spherical micelles with B core and mixed A/C corona. The S' solvent beads are replaced by the S beads in the course of second-step assembly and the corresponding interaction parameters are reset, which are listed in Table S3. In images (a) and (b), the numbers of polymer chains in the spherical micelles are chosen as 30 and 60, respectively.
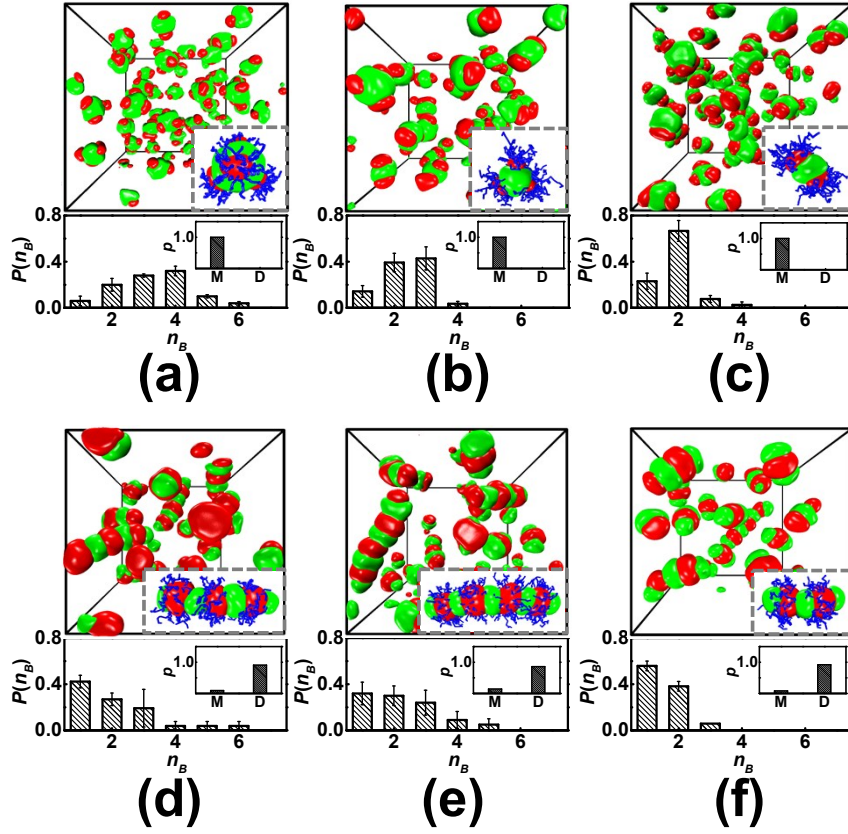
Figure S4. (Upper panels) Self-assembled superstructures of $A_xB_yC_z$ triblock terpolymers with various length ratios x/y of A to B blocks. Insets show typical configurations of triblock terpolymers. (Lower Panels) Probability distribution $P(n_B)$ of B compartment number n_B in each superstructure. The error bars stand for the standard deviations. Insets show probability distribution p of colloidal nanoparticles with various patch numbers in the start-up of second-step assembly. M and D denote the monovalent and divalent colloidal nanoparticles, respectively. (a) $A_{10}B_3C_9$ (corresponds to $PS_{306}PB_{151}PMMA_{340}$ in experiments), (b) $A_{11}B_6C_{10}$ ($PS_{337}PB_{333}PMMA_{369}$), (c) $A_9B_6C_{12}$ ($PS_{277}PB_{333}PMMA_{430}$), (d) $A_{11}B_{14}C_{11}$ ($PS_{363}PB_{765}$ $PMMA_{389}$), (e) $A_9B_{11}C_8$ ($PS_{283}PB_{596}PMMA_{304}$) and (f) $A_{12}B_{15}C_{14}$ ($PS_{374}PB_{819}PMMA_{509}$). The superstructures of $A_xB_yC_z$ triblock terpolymers are obtained from the stepwise self-assembly strategy as shown in Figure1b of main text.

Table S4. Morphological comparisons between the experimental results and the predictions

Experimental results[a]			Predictions		
Sample[b]	v_S/v_B[c]	Morphology[d]	Model[e]	x/y[f]	Morphology
$S_{354}B_{148}M_{352}$	4.20	S	$A_{11}B_3C_{10}$	3.67	S
$S_{306}B_{151}M_{340}$	3.57	S	$A_{10}B_3C_9$	3.33	S
$S_{337}B_{333}M_{369}$	1.78	S	$A_{11}B_6C_{10}$	1.83	S
$S_{660}B_{674}M_{350}$	1.72	S	$A_{21}B_{12}C_9$	1.75	S
$S_{611}B_{635}M_{292}$	1.69	S	$A_{19}B_{12}C_8$	1.58	S
$S_{277}B_{333}M_{430}$	1.46	S	$A_9B_6C_{12}$	1.50	S
$S_{325}B_{681}M_{764}$	0.84	L	$A_{10}B_{13}C_{21}$	0.77	L
$S_{363}B_{765}M_{389}$	0.84	L	$A_{11}B_{14}C_{11}$	0.79	L
$S_{283}B_{596}M_{304}$	0.84	L	$A_9B_{11}C_8$	0.82	L
$S_{374}B_{819}M_{509}$	0.80	L	$A_{12}B_{15}C_{14}$	0.80	L
$S_{141}B_{345}M_{157}$	0.72	L	$A_4B_6C_4$	0.67	L
$S_{283}B_{700}M_{378}$	0.71	L	$A_9B_{13}C_{10}$	0.69	L

a. Experimental results are collected from Ref. S4.

b. Abbreviation SBM represents triblock terpolymer of polystyrene-*block*-polybutadiene-*block*-poly(methylmethacrylate). Subscripts denote number average degrees of polymerization of each blocks.

c. Ratio of volume v_S to v_B is calculated from polymer densities, which are shown in Table S1.

d. Letters S and L represent the spherical and linear multicompartment micelles, respectively.

e. $A_xB_yC_z$ nomenclature corresponds to coarse-grained polymer chain. Subscripts denote bead numbers of A, B and C blocks. Note that the bead numbers are rounded to 'cleaner' numbers in the mapping process.

f. Ratio x/y corresponds to length ratio of solvophobic A to B blocks.
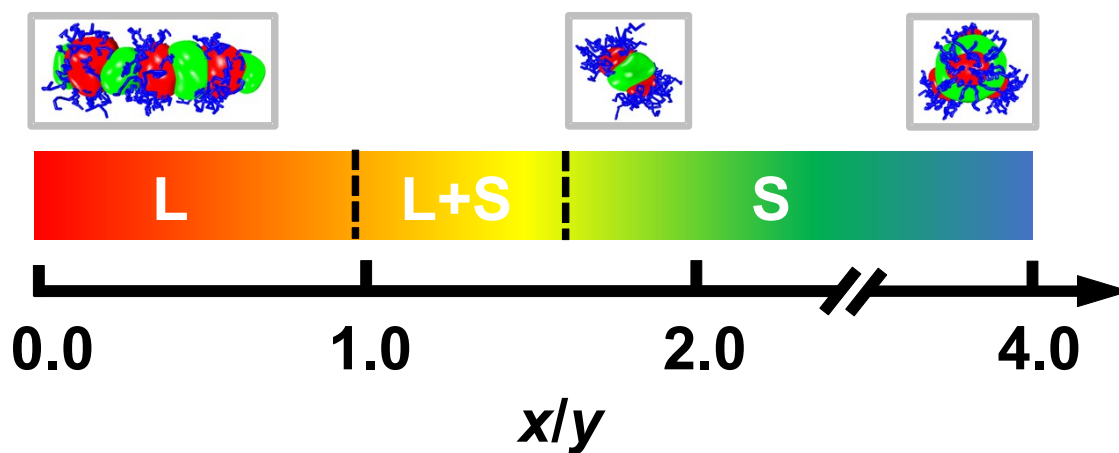
Figure S5. Morphological stability region as a function of the block length ratio x/y of $A_9B_yC_8$ triblock terpolymers. The L and S represent the linear and spherical multicompartment superstructures, respectively. The L+S stands for the mixture of linear and spherical superstructures. Note that one break is applied to the axis for clarity.
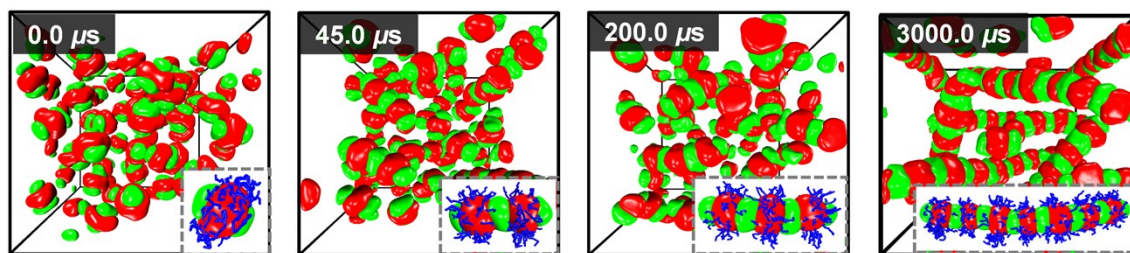
Part D: Self-assembly of colloidal nanoparticles

Figure S6a shows the morphological evolution of superstructures self-assembled from the colloidal nanoparticles of $A_9B_{15}C_8$ triblock terpolymers. In the colloidal monomers, the solvophobic A compartments generate attractions due to unfavorable contacts of A blocks with S solvents, but the solvophilic C blocks produce repulsions to avoid the non-directional aggregations (at time $t=0.0$ μs). To minimize the interfacial energy of system, the divalent colloidal monomers rapidly condense with neighboring nanoparticles *via* attachment of solvophobic A compartments, thereby organizing them into colloidal dimers ($t=45.0$ μs). Therein, the solvophobic A compartments between the two separated B domains act as physical bonds to connect the colloidal monomers, but 'reactivity' of non-attached A compartments at the ends of colloidal dimers is maintained. Subsequently, the colloidal dimers collide with the isolated superstructures and self-assemble into supracolloidal oligomers ($t=200.0$ μs). In the later stage of colloidal self-assembly, coalescence events of supracolloidal oligomers also take place and longer supracolloidal polymers are formed ($t=3000.0$ μs).

The DPD simulations not only permit a visualization of the morphological evolution of supracolloidal polymers, but also provide an opportunity to probe into self-assembly mechanism of colloidal nanoparticles. Figure S6b presents the formation pathways of colloidal dimers by the condensation of divalent colloidal monomers. Two colloidal nanoparticles are separated by a distance in the initial stage of colloidal self-assembly (Snapshot i). The thermal motions of colloidal nanoparticles induce the random collisions with each other. At $t=32.0$ μs, the colloidal nanoparticles collide *via* the side-to-side manner

by the contact of solvophilic C blocks (Snapshot ii). Consequently, the repulsions of C blocks push the colloidal nanoparticles away and prevent the contacts of A patches. Subsequently, the diffusion of colloidal nanoparticles continues (Snapshot iii). Upon the end-to-end collision occurs at t=105.0 μs (Snapshot iv), the solvophobic A patches quickly form the physical bonds to alleviate energetic penalty from the exposure of A patches. This 'reaction' between colloidal nanoparticles occurs in ~10.0 μs and leads to the formation of colloidal dimer at t=115.0 μs (Snapshot v).

Figure S6c shown the formation pathway of supracolloidal polymers by the coalescence of colloidal oligomers. At time t=140.0 μs, the formed dimer are dispersed in the solvents with a distance (Snapshot I). When the colloidal dimers collide *via* the side-to-end manner at time t=255.0 μs, the lateral coverage of C blocks prevents the contact between A patches (Snapshot II). In contrast, when the end-to-end collision happens at time t=380.0 μs (Snapshot III), the 'reaction' between colloidal dimers yields supracolloidal polymer in ~15.0 μs. Since mutual orientations of colloidal dimers are not co-linear, the freshly formed supracolloidal polymer has a zigzag shape at time t=395.0 μs (Snapshot IV). The soft and dynamic features of self-assembled superstructure promote reconfiguration to approach the linear supracolloidal polymer (Snapshot V).
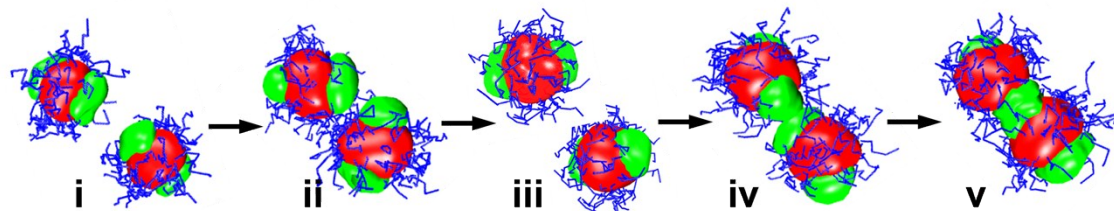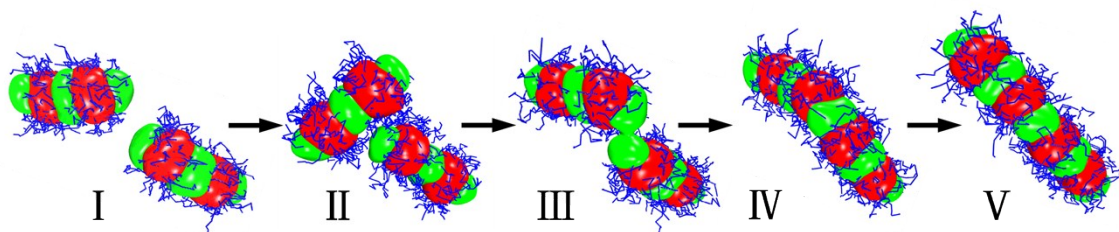
Figure S6. (a) Morphological evolution of superstructures self-assembled from colloidal nanoparticles in S solution. Insets illustrate configuration of triblock terpolymers. (b) Representative snapshots of self-assembled superstructures in the process of monomer condensation. The snapshots are taken for times (i) t=4.0 μs, (ii) t=32.0 μs, (iii) t=60.0 μs, (iv) t=105.0 μs and (v) t=115.0 μs. (c) Formation pathway of supracolloidal polymers by the coalescence of colloidal oligomers. The snapshots are taken for times (I) t=140.0 μs, (II) t=255.0 μs, (III) t=380.0μs, (IV) t=395.0 μs and (V) t=425.0 μs.

Part E: Theoretical model of step-growth polymerization of colloidal nanoparticles

In this Part, we provide the definitions of variables in the formulations of step-growth polymerization (SGP) model and then derive Eq. (2)-(5) in the main text. Our system consists of divalent colloidal nanoparticles with the binding capabilities on their ends, which are equivalent to molecular monomers with two functional groups in the process of polymerization reaction. The extent p of reaction is defined as the ratio of the decreased number (C_0-C) of building units to the initial concentration C_0 of colloidal nanoparticles, $p \equiv (C_0-C)/C_0$ or equivalently $1-p = C/C_0$. The average number $<N>_n$ of colloidal monomers in the supracolloidal polymers is expressed as $<N>_n \equiv C_0/C = 1/(1-p)$.

The consumption of building units obeys the following rate equation

$$\frac{dC}{dt} = -kC^2$$

(S3)

Here, the rate coefficient k can be estimated by the average number $<N>_n$ of colloidal monomers and the exponential factor α (*i.e.*, $k=k_0/<N>_n{}^\alpha$),[S8] where k_0 is the rate constant. The rate equation is rewritten as

$$-\frac{dC}{dt} = k_0 \frac{1}{C_0{}^\alpha} C^{\alpha+2}$$

(S4)

Integrating this expression leads to $\dfrac{1}{\alpha+1}\left(\dfrac{1}{C^{\alpha+1}} - \dfrac{1}{C_0{}^{\alpha+1}}\right) = \dfrac{k_0}{C_0{}^\alpha}t$. Then, the expression of $<N>_n$ is given by

$$\langle N \rangle_n \equiv \frac{C_0}{C} = \left[K_1 t + 1\right]^{\frac{1}{\alpha+1}}$$

(S5)

where $K_1 = (\alpha+1)k_0 C_0$.

According to the most probable distribution principle, the probability of supracolloidal polymers with nanoparticle number i is given by $x_i = p^{i-1}(1-p)$. Thus, the concentration of corresponding superstructures is expressed as $c_i = Cx_i$. On the basis of the relationship $1-p = C/C_0$, the quantity is re-written as $c_i = C_0 p^{i-1}(1-p)^2$. In particular, the concentration of free colloidal nanoparticles corresponds to the case of $i=1$, i.e., $C_m = c_1 = C_0(1-p)^2$. Substituting the formulation $1-p = 1/\langle N \rangle_n$ and Eq. (S5), one can obtain

$$C_m = \frac{C_0}{\langle N \rangle_n^2} = \frac{C_0}{[K_1 t + 1]^{\frac{2}{\alpha+1}}}$$

(S6)

The total concentration of building units includes the contributions from the colloidal nanoparticles and the supracolloidal polymers, i.e., $C = C_m + C_p$. Combining the definition $\langle N \rangle_n \equiv C_0/C$, one can deduce

$$C_p = \frac{C_0}{\langle N \rangle_n} - C_m = \frac{C_0\left[(K_1 t + 1)^{\frac{1}{\alpha+1}} - 1\right]}{(K_1 t + 1)^{\frac{2}{\alpha+1}}}$$

(S7)

The polydispersity index (PDI) of supracolloidal polymers has a relationship with the reaction extent p, $PDI = 1 + p$.[S9] Substituting the formulation $p = 1-1/\langle N \rangle_n$, one can deduce the expression of PDI given by

$$PDI = 2 - \frac{1}{\langle N \rangle_n} = 2 - \frac{1}{[K_1 t + 1]^{\frac{1}{\alpha+1}}}$$

(S8)

Part F: Effects of physiochemical properties of solvophilic C blocks

Figure S7a shows the temporal evolution of the square $\langle N \rangle_n^2$ of average number of colloidal monomers at the interaction parameters a_{CS}=21.0, 24.0 and 27.0. In the case of a_{CS}<25.0, the S beads are good solvents for the C blocks. The polymerization-like kinetics in the system of colloidal nanoparticles obeys the $\langle N \rangle_n^2 \propto t$ relationship. The larger interaction parameter a_{CS} results in a noticeable acceleration of colloidal self-assembly. Figure S7b displays the self-assembly kinetics of colloidal nanoparticles from triblock terpolymers with adjustable length of solvophilic C blocks. As the solvophilic C blocks become long, the colloidal nanoparticles slowly self-assemble into the supracolloidal polymers with smaller aspect ratio.

It should be noted that the fitted curve of simulation data shows a deviation in the later stage of DPD simulations under the condition of a_{CS}=27.0 (Figure S7a). Such deviation is attributed to the formation of branched supracolloidal polymers *via* the manner of end-to-side collisions. Figure S7c displays the formation of branched supracolloidal polymers for the interaction parameter a_{CS}=27.0. Under this condition, the C blocks become collapse to relieve the contacts with the selective S solvents, leading to the retraction of C blocks from the A patches in the supracolloidal polymers (Snapshot i). The exposed A patches is attached laterally by the 'reactive' A compartment at one end of building units (Snapshot ii). The soft and dynamic features of such structures allow the reconfiguration to yield the superstructure with branched topologies (Snapshots iii and iv). The finding highlights the importance of physicochemical properties of triblock terpolymers on the formation pathway of supracolloidal polymers as well as on their shape.
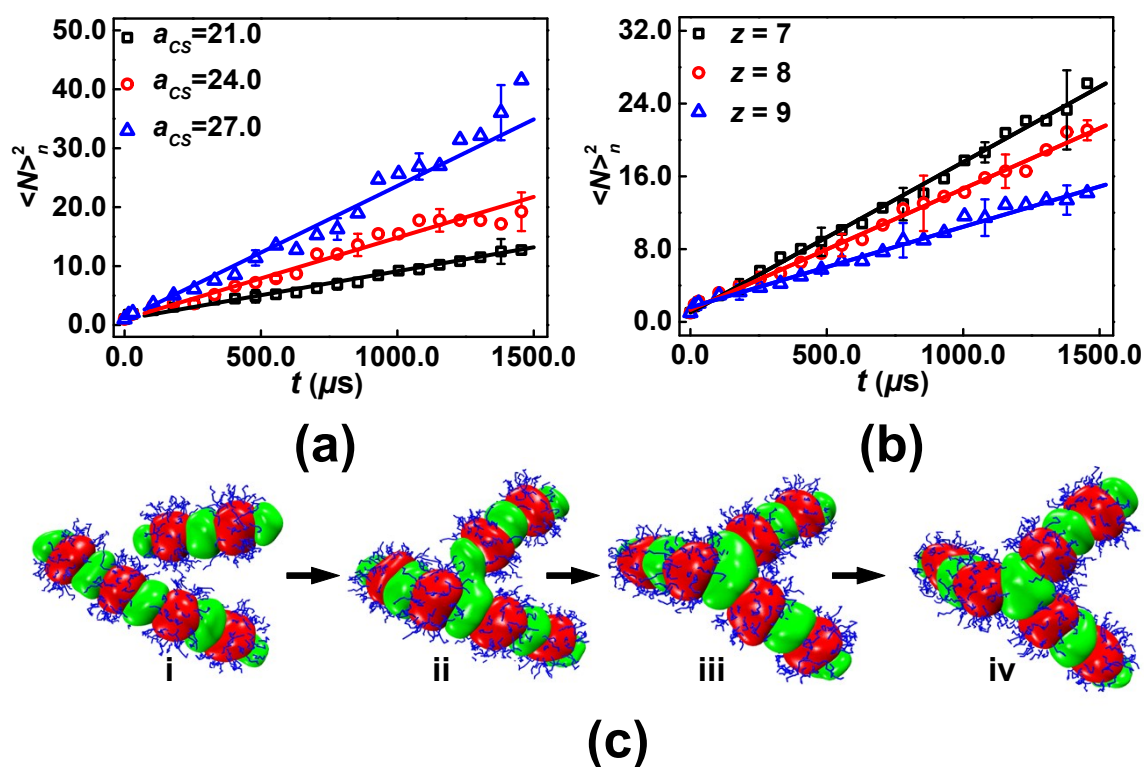
Figure S7. Effects of physiochemical properties of solvophilic C blocks on the polymerization-like kinetics. (a) Temporal evolution of the square $\langle N \rangle_n^2$ of average number of colloidal monomers for various interaction parameters a_{CS} between solvophilic C blocks and S solvent beads. (b) Temporal evolution of the square $\langle N \rangle_n^2$ of average number of colloidal monomers for various lengths z of solvophilic C blocks. The solid lines in panels (a) and (b) represent the best fitted curves according to Eq. (2) of main text. (c) Formation process of branched supracolloidal polymers. The snapshots are taken for time (i) t=543.0 μs, (ii) t=628.0 μs, (iii) t=637.0 μs and (iv) t=646.0 μs.

Part G: Effects of physiochemical properties of solvophobic A and B blocks

We examine the effects of physiochemical properties of solvophobic A blocks on the polymerization-like kinetics, which are depicted in Figure S8. As shown in Figure S8a and S8b, the growth rate K_1 of supracolloidal polymers is inversely proportional to the interaction parameter a_{AS} between A blocks and S beads. The reason can be understood as follows: an increase of a_{AS} boosts the energy cost from the immiscibility between solvophobic A blocks and S beads. To reduce the penalty of interfacial energy, the exposed area S_A of A patches becomes small (Figure S8b), resulting in the lower probability of effective collision of building units or growth rate of supracolloidal polymers. Figure S8c and S8d displays the effect of A block length on the self-assembly kinetics of colloidal nanoparticles constructed from $A_xB_{15}C_8$ triblock terpolymers. As the length of solvophobic A blocks is changed from 8 to 10, the exposed area S_A of terminal A patches or the growth rate of supracolloidal polymers is increased.

The effects of physiochemical properties of solvophobic B blocks on the polymerization-like kinetics are also examined. Figure S9a shows the square $\langle N \rangle_n^2$ of average number of colloidal monomers as a function of the time t for different interaction parameters a_{BS} between the B blocks and the S beads. The self-assembly kinetics of colloidal nanoparticles obeys the step-growth polymerization with variable rate coefficient. As the interaction parameter a_{BS} is tuned, the growth rate K_1 of supracolloidal polymers and the exposed area S_A of terminal A patches have a slight change (Figure S9b). Figure S9c and S9d depicts the effect of the B block length on the self-assembly kinetics of colloidal nanoparticles constructed from the $A_9B_yC_8$ triblock terpolymers. As the B block length y is

varied from 11 to 20, the volume of B domains is increased, leading to the reduction of the coverage of the C corona on the terminal A patches. As a consequence, the exposed area S_A of A patches is increased, leading to an increase in the growth rate K_1 of supracolloidal polymers.
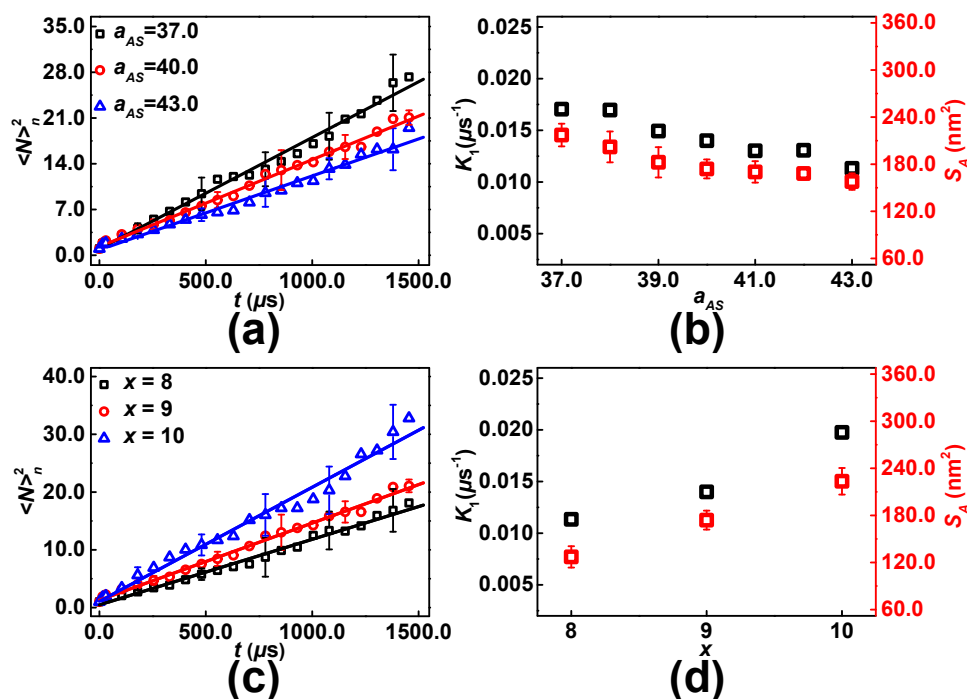

Figure S8. Effect of physiochemical properties of solvophobic A blocks on the polymerization-like kinetics. (a) Temporal evolution of the square $\langle N \rangle_n^2$ of average number of colloidal monomers in the course of colloidal self-assembly for various interaction parameters a_{AS} between the solvophobic A blocks and S beads. (b) Growth rate K_1 of supracolloidal polymers and exposed area S_A of terminal A patches as a function of the interaction parameter a_{AS}. (c) Temporal evolution of the square $\langle N \rangle_n^2$ of average number of colloidal monomers for various length x of solvophobic A blocks. (d) Growth rate K_1 of supracolloidal polymers and exposed area S_A of terminal A patches as a function of the length x of solvophobic A blocks. The solid lines represent the best fitted curves on the basis of Eq. (2) in the main text.
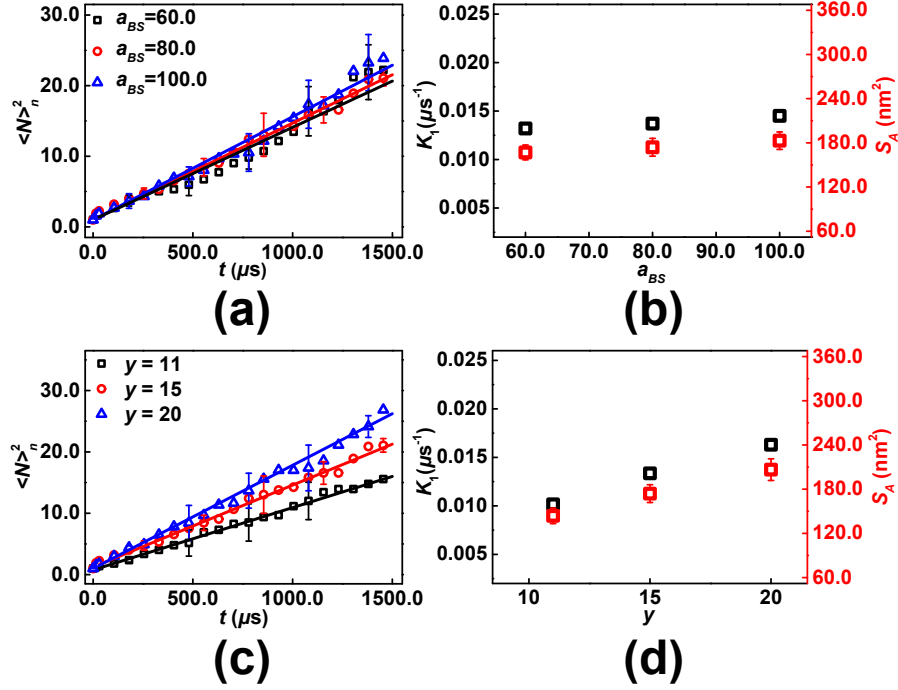
Figure S9. Effects of physiochemical properties of solvophobic B blocks on the polymerization-like kinetics. (a) Temporal evolution of the square $\langle N \rangle_n^2$ of average number of colloidal monomers for various interaction parameters a_{BS} between the solvophobic B blocks and the S beads. (b) Growth rate K_1 of supracolloidal polymers and exposed area S_A of terminal A patches as a function of the interaction parameter a_{BS}. (c) Temporal evolution of the square $\langle N \rangle_n^2$ of average number of colloidal monomers for various lengths y of solvophobic B blocks. (d) Growth rate K_1 of supracolloidal polymers and exposed area S_A of terminal A patches as a function of the length y of solvophobic B blocks. The solid lines represent the best fitted curves on the basis of Eq. (2) in the main text.

Part H: Self-assembly kinetics of homopolymer-functionalized nanoparticles

In this part, we perform additional simulations on self-assembly of solid nanoparticles with hairy patches, which are composed of rigid cylinder and polymer molecules at the ends (Figure S10a). The settings of interaction parameters are derived from the experimental work of Kumacheva and co-authors (*i.e.*, the polymer molecules are solvophobic and the rigid cylinder is solvophilic due to the existence of lateral bilayer of cetyl trimethyl ammonium bromide).[S14] The hairy nanoparticles are spontaneously connected by the solvophobic polymer molecules, resulting in the formation of nanoparticle chains (Figure S10b). As illustrated in Figure S10c, the average number $<N>_n$ of hairy nanoparticles in each chain as a function of time t satisfies the relationship $<N>_n \sim t$, which corresponds to the classic step-growth polymerization model with constant rate coefficient (*i.e.*, the modified Flory's equation with exponential factor $\alpha=0$ in the main text). These findings reproduce the step-growth polymerization kinetics of inorganic nanoparticles, validating our computational model.

To elucidate the origin of the difference (*i.e.*, $<N>_n \sim t$ for hairy nanoparticles and $<N>_n^2 \sim t$ for soft colloidal nanoparticles), we introduce persistence length to evaluate the flexibility of nanoparticle chains. The persistence length l_p is defined as projection of end-to-end vector **R** on the principal axis $\mathbf{r}_1$ of first nanoparticle (Figure S10d).[S10] As shown in Figure S10e, the persistence length of hairy nanoparticle chains is much lower than that of supracolloidal polymers, indicating that the hairy nanoparticle chains are more flexible than the supracolloidal polymers. As a result, the end-to-end collisions of flexible hairy nanoparticle chains do not require the motion of whole chains,[S11] leading to the constant rate coefficient in the step-growth polymerization model. In contrast, the end-to-end collisions of supracolloidal

polymers require the translation and rotation of whole superstructures, resulting in the size dependence of rate coefficient.

To further elucidate the role of rigid nanoparticles on the polymerization-like kinetics, we perform additional simulations on the self-assembly behavior of rigid nanoparticles. Herein, the interaction parameters between different types of beads are the same as the case of Figure 3 in the main text, but the colloidal nanoparticles are fixed as rigid bodies (*i.e.*, the polymer chains in the nanoparticles are fixed, but the motion of nanoparticles obeys the dynamics of rigid bodies). Such rigid nanoparticles self-assemble into the linear supracolloidal polymers, which are similar to the configurations shown in Figure S6. The square $\langle N \rangle_n^2$ of average number of rigid nanoparticles in each supracolloidal polymers linearly increases with the assembly time t (Figure S10c), which is a qualitative feature of diffusion-controlled step-growth polymerization kinetics.
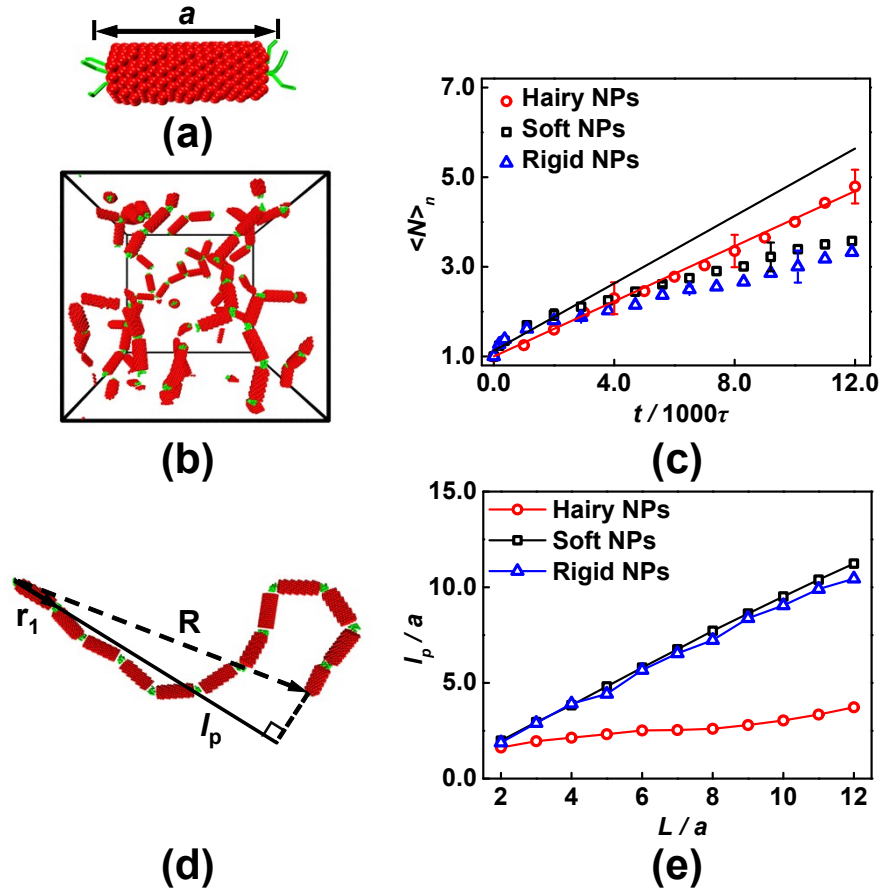
Figure S10. (a) Model of hairy nanoparticle consisting of rigid cylinder and polymer molecules at the ends. a represents the characteristic length of nanoparticle. (b) Snapshot of self-assembled structures of hairy nanoparticle at $1.2 \times 10^4 \tau$. τ is the time unit of simulations. (c) Average number $<N>_n$ of nanoparticles in each chain as a function of time in the course of assembly of hairy nanoparticles (hairy NPs) and soft/rigid colloidal nanoparticles (soft NPs, corresponding to the case of main text, and rigid NPs). The solid lines represent the fitted curves on the basis of the step-growth polymerization model with exponential factors $\alpha=0$. (d) Definition of persistence length l_p of a single chain. $\mathbf{R}$ is the end-to-end vector and $\mathbf{r}_1$ is the principal axis of first nanoparticle. (e) Persistence length of nanoparticle chains as a function of their length L. The lengths of nanoparticle chains are rescaled by characteristic length a of respective nanoparticles.

Part I: Effects of preparation process on self-assembly kinetics

To evaluate the effect of preparation process on the self-assembly kinetics of colloidal nanoparticles, we build upon annealing process to mimic the dialysis process of spherical micelles in a good solvent (designated as S') against a poor (S) in the second-step assembly.[S12, S13] In the annealing simulations, the interaction parameter between A blocks and solvent beads is changed from $a_{AS'} = 27.9$ to $a_{AS} = 40.0$ following the linear schedule, $a_{AS}(t) = a_{AS'} + (a_{AS} - a_{AS'})t/t_A$ (top panel of Figure S11a), where $a_{AS}(t)$ is the interaction parameter at time t and t_A is the annealing time. It should be noted that case of $t_A = 0.0~\mu$s corresponds to our quenching simulations in the main text.

Bottom panel of Figure S11a shows the self-assembly kinetics of nanoparticles under various annealing times t_A. In the case of rapid annealing (*e.g.*, $t_A = 45.0~\mu$s), square $\langle N \rangle_n^2$ of average number of colloidal nanoparticles in each supracolloidal polymer linearly increases with time, which is extremely similar to the case of $t_A = 0.0~\mu$s. However, as the annealing time becomes long (*e.g.*, $t_A = 750.0~\mu$s), different scenarios are observed. In the initial stage of annealing simulation, the A blocks become collapse and form loose patches on the nanoparticles due to their weak solvophobicity (Figure S11b-i). Meanwhile, the secondary assembly of nanoparticles is triggered for reduction of interface energy. Because of the larger exposed area of loose patches, the assembly rate of nanoparticles is higher than the cases of $t_A = 0.0$ and $45.0~\mu$s. Beyond the annealing time ($t_A > 750.0~\mu$s), the loose patches become dense to minimize the energy contribution from unfavorable A patch/solvent interfaces. As a result, the growth rate of supracolloidal polymers is suppressed, and is slight higher than the cases of $t_A = 0.0$ and $45.0~\mu$s. It should be pointed out that the finally assembled superstructures consist

of branching (highlighted by arrows in Figure S11b-ii). As illustrated above, the dialysis process affects the formation of nanoparticles. After the dialysis process, the assembly kinetics of nanoparticles is similar to the case of quenching simulations in the main text.
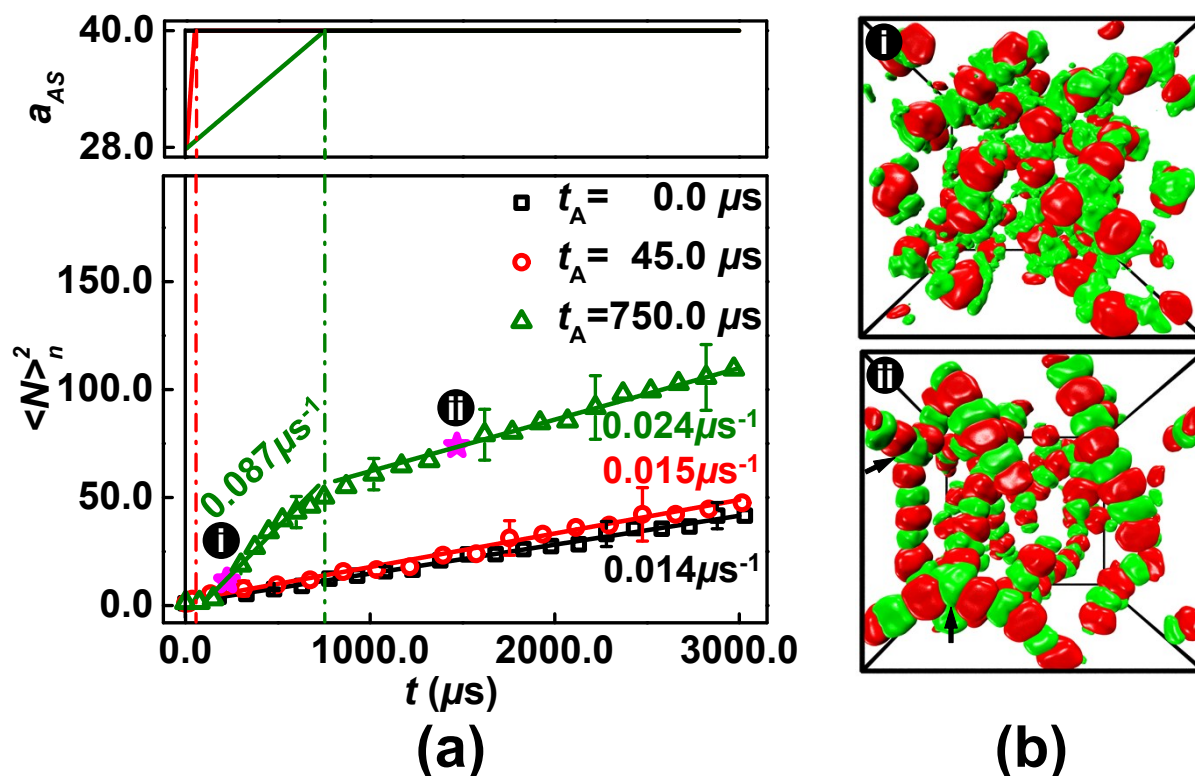

(a)

(b)

Figure S11. (a) Top panel: Interaction parameter a_{AS} between A blocks and solvent beads as a function of time. Bottom panel: Square $\langle N \rangle_n^2$ of average number of colloidal nanoparticles as a function of time under various annealing times. The growth rates of supracolloidal polymers are annotated. (b) Snapshots of assembled superstructures of nanoparticles for the case of annealing time $t_A=750.0$ μs. The Roman numbers match the labels in panel (a). The arrows highlight the branching of supracolloidal polymers.

Part J: Self-assembly kinetics of triblock terpolymers in various strategies

As stated in the main text, the monodisperse colloidal nanoparticles with the chain number n_{chain}=60 of triblock terpolymers are chosen as the initial configuration of simulations at the second-step assembly. As a comparison, we also simulate the formation of superstructures, starting from the initial configuration of polydisperse colloidal nanoparticles at the second-step assembly or triblock terpolymers randomly dispersed in the S solvents *via* the one-step assembly. The evolution and formation kinetics of superstructures from various self-assembly strategies are illustrated in Figure S12 and S13.

In the case of stepwise self-assembly strategy, the $A_9B_{15}C_8$ triblock terpolymers self-associate into the polydisperse spherical micelles with the chain number in the range of $20 \leq n_{chain} \leq 120$, which are demonstrated in Figure S12a. After change of solvent quality at the start-up of second-step assembly, the spherical micelles evolve into the anisotropic colloidal nanoparticles with distinct valences, strongly depending upon the chain number (inset of Figure S12a). Subsequently, mixture of monovalent and divalent colloidal nanoparticles undergoes next-level assembly to form the supracolloidal polymers. However, their formation pathway may be altered due to existence of monovalent colloidal nanoparticles. As shown in Figure S12b, one end of superstructures is capped by the monovalent colloidal nanoparticles (Snapshots i and ii), leading to the lower 'reactivity' of building units. Furthermore, the supracolloidal polymers loss their 'reactivity' when both ends are capped by the monovalent colloidal nanoparticles (Snapshots iii and iv). These phenomena can be quantitatively verified by the $\langle N \rangle_n^2 \sim t$ plot as shown in Figure S12c. In particular, the growth rate of supracolloidal polymers is markedly lowered due to a reduction of the number of divalent colloidal

nanoparticles, and the polymerization-like kinetics deviates from our proposed model in the later stage of simulations. In addition, the chain number n_{chain} in each B compartment generally remains constant during the self-assembly of colloidal nanoparticles (Figure S12d), implying that the fusion event of B compartments rarely occurs.

The simulations of one-step self-assembly start from the configuration of triblock terpolymers randomly dispersed in S solvents. Figure S13 shows the morphological evolution of self-assembled superstructures from one-step assembly strategy. In the initial stage, the triblock terpolymers self-assemble into small ill-defined aggregates with distinct sizes of A and B cores (Snapshot a). In the intermediate stage, small aggregates gradually fuse into chain-like superstructures, where the solvophobic A and B compartments have various sizes (Snapshot b). This may lead to the formation of branched superstructures (highlighted by arrow in Snapshot c). In the later stage, the triblock terpolymers self-assemble into the superstructures with the linear shape, which are similar to the supracolloidal polymers obtained from the stepwise self-assembly strategy. However, such superstructures have higher branching (Snapshot d), and their internal A and B compartments has different sizes, originating from the structural inhomogeneity of small aggregates at the initial stage of self-assembly of triblock terpolymers.

As shown in Figure S12c, the values of $\langle N \rangle_n^2$ are not linearly proportional to the time t, implying that the growth of superstructures does not obey the step-growth polymerization kinetics. Such deviation originates from the fusion of B compartments in the course of self-assembly of triblock terpolymers (Figure S12d). Moreover, the chain number n_{chain} of triblock terpolymers in the B compartments has a wider distribution than that of stepwise self-

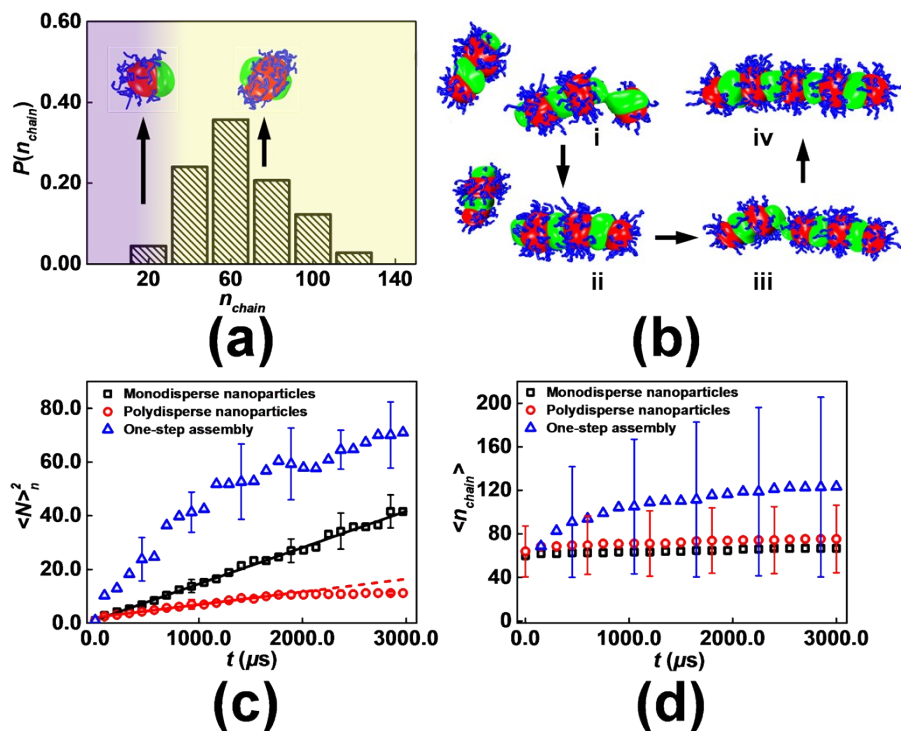assembly (error bars in Figure S12d).

Figure S12. (a) Probability distribution $P(n_{chain})$ of chain number n_{chain} in each pre-assembled

micelle. Insets represent typical configurations of nanostructures at early stage of second-step

assembly for the pre-assembled micelles at given chain number. (b) Representative snapshots

of superstructures in the course of self-assembly of polydisperse colloidal nanoparticles. The

snapshots are taken for time (i) t=1895.0 μs, (ii) t= 1906.0 μs, (iii) t=2531.0 μs and (iv)

t=2545.0 μs. (c) Square $\langle N \rangle_n^2$ of average number of colloidal monomer in supracolloidal

polymers as a function of the time t for different self-assembly strategies: (□) self-assembly

of monodisperse colloidal nanoparticles, (○) self-assembly of polydisperse colloidal

nanoparticles and (Δ) one-step self-assembly of triblock terpolymers dispersed in S solvents.

The lines represent the fitted curves based on the step-growth polymerization model with

exponential factor α=1. (d) Average number $\langle n_{chain} \rangle$ of polymer chains in each B

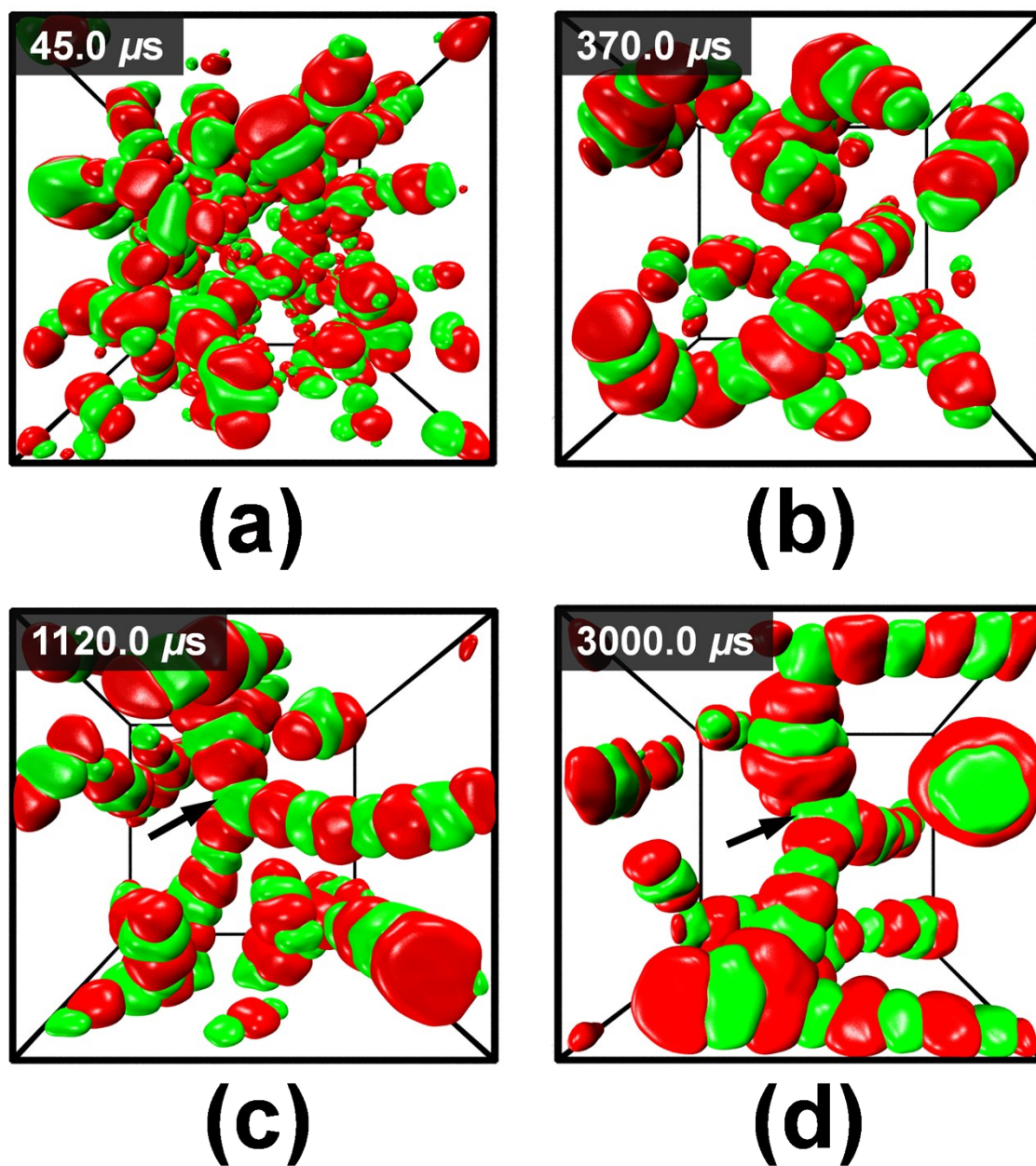compartment as a function of the time t for different self-assembly strategies.

Figure S13. Morphological evolution of self-assembled structures of triblock terpolymers dispersed in the S solvents. The times are (a) t=45.0 μs, (b) t=370.0 μs, (c) t=1120.0 μs, (d) t=3000.0 μs. The arrows highlight the branched points of supracolloidal polymers.

References

(S) R. Groot and P. Warren, *J. Chem. Phys.*, 1997, **107**, 4423−4435.

(S2) A. Maiti and S. McGrother, *J. Chem. Phys.*, 2004, **120**, 1594−1601.

(S3) W. Lee, S. Ju, Y. Wang and J. Chang, *J. Chem. Phys.*, 2007, **127**. 064902.

(S4) A. H. Gröschel, F. H. Schacher, H. Schmalz, O. V. Borisov, E. B. Zhulina, A. Walther and A. H. E. Müller, *Nat. Commun.*, 2012, **3**, 710.

(S5) R. D. Groot and K. L. Rabone, *Biophys. J.*, 2001, **81**, 725−736.

(S6) J. E. Mark, *Physical Properties of Polymers Handbook*, 2nd ed, Springer, 2007.

(S7) Z. Li and E. E. Dormidontova, *Macromolecules*, 2010, **43**, 3521–3531.

(S8) C. Ribeiro, E. J. H. Lee, E. Longo and E. R. Leite, *ChemPhysChem*, 2006, **7**, 664−670.

(S9) G. Odian, *Principles of Polymerization*, John Wiley & Sons, Inc., Hoboken, 4th edn, 2004.

(S10) M. Ullner and C. E. Woodward, *Macromolecules*, 2002, **35**, 1437−1445.

(S11) P. J. Flory, *Principles of Polymer Chemistry*, Cornell University Press, Ithaca, 1953.

(S12) A. A. Rudov, E. S. Patyukova, I. V. Neratova, P. G. Khalatur, D. Posselt, C. M. Papadakis and I. I. Potemkin, *Macromolecules*, 2013, **46**, 5786−5795.

(S13) B. Yu, P. Sun, T. Chen, Q. Jin, D. Ding and B. Li, *Phys. Rev. Lett.*, 2006, **96**, 138306.

(S14) K. Liu, Z. Nie, N. Zhao, W. Li, M. Rubinstein and E. Kumacheva, *Science*, 2010, **329**, 197–200.